RESEARCH ARTICLE | MAY 08 2025

Two-dimensional electronic spectroscopy of Betaine-30

Special Collection: David Jonas Festschrift

Stephen R. Meech ; James N. Bull ; Giovanni Bressan

J. Chem. Phys. 162, 184302 (2025)
https://doi.org/10.1063/5.0268084

The Journal of Chemical Physics ARTICLE pubs.aip.org/aip/jcp

Two-dimensional electronic spectroscopy of Betaine-30

Cite as: J. Chem. Phys. 162, 184302 (2025); doi: 10.1063/5.0268084
Submitted: 27 February 2025 • Accepted: 21 April 2025 •
Published Online: 8 May 2025

Stephen R. Meech, James N. Bull, and Giovanni Bressan[a]

AFFILIATIONS

School of Chemistry, University of East Anglia, Norwich NR4 7TJ, United Kingdom

Note: This paper is part of the JCP Special Topic, David Jonas Festschrift.
[a]**Author to whom correspondence should be addressed:** g.bressan@uea.ac.uk

ABSTRACT

Betaine-30 is well-established as a standard dye for solvatochromism and has long been studied by ultrafast spectroscopy. Electronic excitation leads to rapid intramolecular electron transfer, while the decay of the resulting state corresponds to back electron transfer to the electronic ground state. Thus, Betaine-30's photophysics offers a route to probing the role that vibrational excitation and solvent dynamics play in electron transfer reaction rates. Here, we probe the excited state dynamics of Betaine-30 in two solvents (ethanol and acetonitrile) by means of two-dimensional electronic spectroscopy. Population dynamics in ethanol are measured at two pump wavelengths, and global analysis reveals a wavelength dependence of the electron transfer rate. This is assigned to excitation of distinct ground state conformers, which is confirmed by quantum chemical calculations. "Beatmaps" of coherently excited vibrations are recovered and analyzed in terms of the contribution of Raman active modes in ground and excited states. The contribution of modes in the excited state is a strong function of the rate of the electron transfer reaction.

INTRODUCTION

The pyridinium *N*-phenolate dye Betaine-30 (B30) was first synthesized more than sixty years ago by Reichardt *et al.* and has received a lot of attention because of its strong solvatochromism combined with high solubility and photostability.[1] Its solvatochromic properties arise from a large difference, $\Delta\mu$, between the magnitude and direction of its ground and excited state permanent dipole moments, μ_g and μ_e (15 and −6 D, respectively).[1] The polar charge-separated ground state S_0 is stabilized by large dielectric constant (ε_r) environments, resulting in a blueshift of the S_0–S_1 transition as a function of the solvent polarity, as the S_1 excited state has a less pronounced dipolar character and is hence stabilized to a smaller extent.

B30 has been extensively studied by ultrafast electronic and vibrational spectroscopies in the past decades,[1–5] and its photoinduced dynamics were rationalized in a 4-level scheme proposed by Kovalenko *et al.*[4] and generalized by Duvanel *et al.*:[6] Electronic excitation of the zwitterionic[6] S_0 state populates the Franck–Condon (FC) region of the S_1 state, whose relaxation is driven by torsion about the bond linking the phenolate and pyridinium rings [see Figs. 1(b) and 1(c)] and polar solvent reorientation. This is accompanied by a substantial decrease (and sign reversal) in μ_e with respect to μ_g; the process is thus referred to as intramolecular electron transfer (iET). The reported iET time constants display a marked solvent dependence, ranging from sub-100 fs in MeCN to 1 ps in short-chain alcohols and ≈10 ps in ethylene glycol. iET is followed by a slower back electron transfer (bET) promoted by structural dynamics, leading to internal conversion (IC), to populate a vibrationally hot ground state (HGS), which ultimately refills the GS over tens of ps via vibrational cooling (VC) and intramolecular vibrational energy redistribution (IVR).

As the rates of iET and bET are orders of magnitude faster than predicted by the classical Marcus model, photoinduced dynamics of B30 have been rationalized based on ET models accounting for solvent friction and classical low frequency and quantized high frequency molecular vibrations.[5,7–9] As the ground and excited states of B30 have strongly coupled nonadiabatic potential energy surfaces (PESs), the role of molecular vibrations on its photoinduced dynamics has been the subject of a number of experimental studies. Hogiu *et al.* used time-resolved coherent anti-Stokes Raman to demonstrate that the bET reaction leaves the GS product in a

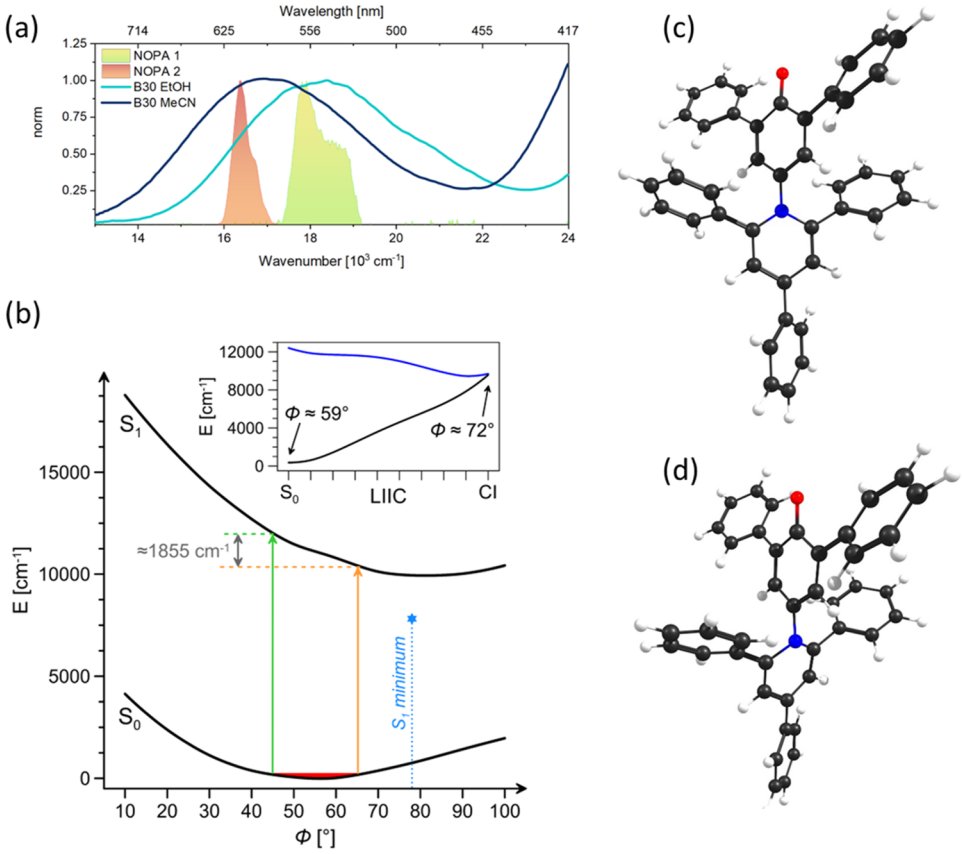

FIG. 1. (a) Normalized steady-state absorption spectra of Betaine-30 (B30) in ethanol (EtOH) and acetonitrile (MeCN) are represented by light and dark blue, respectively. Pump spectra used for HB2DES experiments are represented by green and orange shades, respectively. (b) Potential energy surfaces for torsion (ø) about central N–C bond calculated in the MRSF-TDDFT framework. The inset shows the linear interpolation between the Franck–Condon (S_0) geometry and conical intersection (CI) geometry. (c) Illustration of the optimized S_0 geometry with ø = 59°. (d) Illustration of the conical intersection geometry (<0.02 meV S_1–S_0 separation) with ø = 72°. The relative energy of the S_1 equilibrium geometry is indicated by the blue star in PANEL (b).

vibrationally hot state with respect to high frequency (≈1600 cm^{-1}) modes.[43] Rafiq *et al.* and Ruchira Silva *et al.* respectively, concluded that coupled low frequency torsional modes tune the reactive PES while high frequency vibrations increase the total amount of possible pathways for the bET, which is ultimately incoherent.[2,5]

In the present study, we report a two-dimensional electronic spectroscopy (2DES) study of B30 in polar protic ethanol (EtOH, ε_r = 24.5) and aprotic polar acetonitrile (MeCN, ε_r = 37.5) solvents. 2DES was first demonstrated by Jonas and coworkers[10] in the fully noncollinear degenerate BOXCARS design. Subsequently, 2DES has emerged as an ideal method for the investigation of ultrafast and coherent dynamics in condensed-phase systems as it provides simultaneous access to the excitation (pump, $\tilde{\nu}_1$) and detection (probe, $\tilde{\nu}_3$) frequency dimensions, coupled to high time (few 10s of fs) resolution. Its unique advantages enabled the direct observation of excitonic couplings, spectral diffusion, ultrafast energy and electron transfer, wavepacket dynamics in (supra)molecular systems, photoactive materials, and light-harvesting complexes, among others.[11–18] In 2DES, a pair of fs time-ordered pulses prepares populations and coherent superpositions of electronic or vibronic states, probed by a delayed visible pulse, which is, in the "half-broadband (HB)" design applied here, a white-light continuum (WLC).[19–21] The WLC probe used in HB2DES allowed us to recover population dynamics and ground and excited state vibrational coherences of photoexcited B30 across the whole visible range and to investigate the roles of inhomogeneous broadening and vibrational wavepackets on its ultrafast photoinduced dynamics.

EXPERIMENTAL METHODS

Steady state UV–vis spectra were recorded in static 10 mm fused silica cells in a Perkin–Elmer Lambda XLS benchtop instrument.

HB2DES data were acquired in 0.5 mm optical path static fused silica cells (Starna), with the concentration of B30 adjusted to a peak OD of 0.45 in EtOH and MeCN at 555 and 605 nm, respectively. Sample and solvents were used as received. The home-built half broadband 2D experimental setup was previously described in detail.[19] 500 μJ pulses from the output of a Ti:Sa regenerative amplifier (Spitfire Ace, Spectra-Physics) operating at 800 nm and 1 kHz repetition rate pump a commercial noncollinear optical parametric amplifier (NOPA, Topas White, Light Conversion) to generate broadband pulses centered at either 550 (18 200 cm^{-1}) or 615 nm (16 200 cm^{-1}). The NOPA output (≈500 nJ energy per pulse pair) is precompressed by a commercial folded grism compressor (Fastlite) to achieve close to Fourier transform limited pulses at the sample position. Downstream, a pair of pump pulses with programmable time delay (coherence time τ) and a relative carrier-envelope phase is created in a commercial acousto-optical programmable dispersive filter (AOPDF, Dazzler, Fastlite). The coherence time is scanned shot-to-shot from −95 to 0 fs in 792 as steps. Real and imaginary parts

of the rephasing and nonrephasing 2D responses are obtained by using a 3 × 1 phase-cycling method and summed to obtain absorptive 2D spectra.[22] Each 2D spectrum is averaged over 720 laser shots per value of τ. The waiting time T is introduced by scanning the pump pair-probe delay with a retroreflector mounted on a mechanical delay stage (Physik Instrumente). Data are measured with 15 fs steps from 0 to 1800 fs to record vibrationally coherent dynamics or at increasing T steps between 0 and 10 ps for the population measurements. The probe pulse (WLC) is generated by focusing ≈1 μJ of the 800 nm regenerative amplifier output into a 3 mm static sapphire plate and spans 13 500–23 000 cm^{-1}. The WLC is compressed by two pairs of dispersive mirrors at 5° and 19° angles of incidence (PC 1332, Ultrafast Innovations) and split by a 50:50 beam splitter to provide probe and reference. The probe is crossed at 4° with the collinear pump pair at the sample position. Pump and probe spot sizes are 80 and 160 μm, respectively. Pump pulse energy and duration at sample position are ≈200 nJ and 35 fs, respectively. The signal is recollimated after the sample and the signal and reference are focused into a home-built dual channel prism-based spectrometer and recorded shot-to-shot by a pair of 1024 pixels CCD detectors (Stresing) synchronized to the AOPDF. The signal is referenced using an active noise reduction method proposed by Feng *et al.*[23] The instrument response function (~50 fs, see the supplementary material, Fig. S1) is measured by spectrally resolving the instantaneous nonresonant solvent response. All the measurements were measured at parallel pump(s)–probe polarization to maximize the weak nonlinear signals.

COMPUTATIONAL METHODS

Potential energy surfaces and critical points of isolated B30 were described using a combination of XTB[24] and mixed-reference spin-flip time-dependent DFT (MRSF-TDDFT)[25] using ORCA 6.0.1 and GAMESS-US (June 2023 R2 release).[26,27] First, GOAT (global geometry optimization and ensemble generator) was used to determine the lowest energy (vacuum) conformations of B30. The lowest energy conformation was reoptimized at the BH & HLYP/cc-pVDZ level of theory within the MRSF-TDDFT framework.[28,29] The BH & HLYP functional was chosen because of the high fraction of Hartree–Fock exchange (50%) required for the treatment of charge-transfer states and for suitability with the spin-flip formalism. This method is suited to describing PES regions near conical intersections and in instances where there is substantial charge-transfer character, as is the case for B30. The fully relaxed S_1 geometry and conical intersection (CI) along the S_0–S_1 conical intersection seam were located using analytical gradients with MRSF-TDDFT. LIIC (linear interpolation of internal coordinates) was constructed between the S_0 and CI geometries.

Raman frequencies for gas-phase B30 were computed with the HF-3c Hamiltonian,[30] which is a fast Hartree–Fock based method including selected dispersion, basis set superposition error, and short-range finite basis set corrections.

RESULTS AND DISCUSSION

Steady-state spectroscopy and quantum chemical calculations

Absorption spectra of B30 in acetonitrile (MeCN) and ethanol (EtOH) are shown in Fig. 1(a). Spectra in both solvents are broad (≈5000 cm^{-1} FWHM from Gaussian fit) and featureless. These bands arise from the charge transfer (CT) transition with $|\mu_g| > |\mu_e|$ and hence display negative solvatochromism.[1] Absorption maxima are located at 17 200 and at 18 500 cm^{-1} in MeCN and EtOH, respectively. The breadth of the room-temperature absorption spectrum has been considered in earlier studies[1,31] and was attributed to a distribution of populated conformations combined with different hydrogen-bonding interactions (in alcohols). To further inform on the absorption profile and excited states of B30, we performed quantum chemical calculations shown in Figs. 1(b)–1(d). The substantial size of B30 (72 atoms) means that excited state calculations with meaningful (i.e., explicit) solvation is prohibitively expensive.[32] The PES for S_0 has a shallow minimum with the central N–C dihedral angle, ø, at 59°. We note that this angle differs substantially (by more than 20°) from earlier calculations using an approximate model of B30, omitting the pendant aromatic groups.[33] Such discrepancy suggests that the simple pyridinium–phenolate model is not capable of yielding adequate predictions of the structural changes induced by photoexcitation in B30. The shallow character of the S_0 PES with respect to ø is consistent with a large range of populated geometries (i.e., ø angles spanning nearly 20°) within kT, as indicated by the red shading in Fig. 1(b). Conversely, the S_1 PES has a much steeper gradient with respect to ø over the Franck–Condon region, leading to the broadened absorption spectrum. The calculated vertical S_0–S_1 transition wavelength at the equilibrium geometry in vacuum is ≈830 nm, in good agreement with the absorption maximum of B30 in nonpolar (ε_r = 2.38) toluene at 840 nm.[1] Analysis of the orbitals from the MRSF-TDDFT calculations indicate that the S_0–S_2 electronic transition does not display substantial CT character and lies much further toward the blue (≈440 nm), consistent with the band onset evident at the short wavelength in Fig. 1(a) for both solvents. The unrelaxed S_1 state reaches minimum energy at ø ≈ 80° but does not come close in energy to the S_0 state. Geometry optimization of the S_1 state produced a structure (ø = 78°) situated 7800 cm^{-1} above the S_0 equilibrium geometry [blue star in Fig. 1(b)] and involves stretching of bonds in the aromatic rings as part of the N–C coordinate. The optimized minimum energy crossing point is situated ≈2000 cm^{-1} above the S_1 optimized geometry with ø = 72° and pyramidalization of the N–C coordinate [Fig. 1(d)], with the latter being critical to achieve curve crossing between the S_0 and S_1 PESs. The linear interpolation of internal coordinates (LIIC) extrapolation between the Franck–Condon geometry and minimum energy crossing point (MECP) is shown in the inset of Fig. 1(b) and suggests a barrierless pathway to internal conversion (i.e., to bET) in the gas phase.

The experimental absorption spectra and the prediction from the calculation that more twisted B30 conformations are associated with a redshifted absorption suggests that excitation wavelength resolved measurements might be significant. Here, HB2DES in EtOH were measured using photoexcitation at two different wavelengths [pump spectra labeled as NOPA 1 and 2 in Fig. 1(a)] to investigate inhomogeneous broadening in ethanol and with NOPA 2 only in MeCN (in which case, NOPA 2 data in MeCN and NOPA 1 data in EtOH have similar excess energies, so can be compared).

HB2DES of B30 in EtOH, "NOPA1" excitation

Evolution of 2D absorptive spectra of B30 in EtOH after photoexcitation centered at 18 000 cm^{-1} (NOPA 1) is shown in Fig. 2.

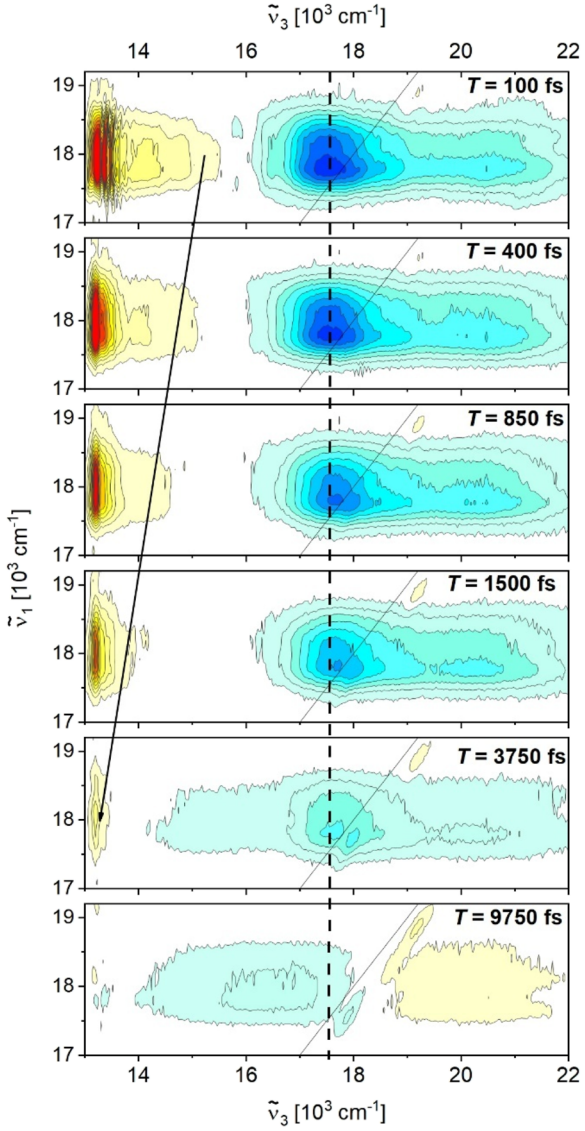

FIG. 2. Absorptive HB2DES spectra of B30 in EtOH after excitation at 18 000 cm^{-1} at selected waiting time values between 0.1 and 9.75 ps. The intensity is given by 21 contour lines; positive signals are shown in yellow, and negative signals are shown in blue. All spectra are normalized to the negative ESA amplitude at T = 0.1 ps. The vertical dash line is a guide to the eye to resolve the spectral shift (see text).

The earliest spectrum at T = 100 fs shows positive weak stimulated emission (SE) peaked toward the red edge of the probe and extending to 15 800 cm^{-1} and a broad negative excited state absorption (ESA) with a sharp strong feature at 17 600 cm^{-1} and a shoulder at 20 500 cm^{-1} extending to $\tilde{\nu}_3$ > 22 000 cm^{-1}. No positive ground state bleach (GSB) signal on the diagonal is detected due to overlap with the strong ESA. The ESA peak becomes rounder over the first couple of hundred fs, which we assign to fast spectral diffusion. The fast time scale of this antidiagonal broadening suggests that its origin lies in ultrafast nondiffusive (librational) solvation dynamics and aligns with the 210 fs value obtained for the fastest solvation dynamics in EtOH by Maroncelli *et al.* from time-resolved fluorescence.[34] We also note that this agrees with the fastest fluorescence decaying component reported by Duvanel *et al.*[6] Over the first 1.5 ps, the ESA shows a minor amplitude decay and ≈400 cm^{-1} blueshift (see vertical dashes) accompanied by a ≈2000 cm^{-1} SE redshift (which is highlighted by an arrow; note that our observation window is limited by the red edge of the WLC at 13 000 cm^{-1}), which also decays in amplitude. Between 2 and 10 ps, the ESA amplitude continues to decay, while a broad, weak negative feature emerges at 16 000 cm^{-1}. A positive GSB feature, previously masked by the strong ESA signal, becomes apparent for T > 7 ps, between 18 500 and 22 000 cm^{-1}. The appearance of the new negative absorption band at 16 000 cm^{-1}, along with the slower GSB refilling, suggests that the initial product of bET is a hot ground state (HGS) with redshifted $S_1 \leftarrow S_0$, which subsequently repopulates the original ground state, consistent with Duvanel *et al.*[6] Weak signals in the few ps range are convoluted with pump scatter artifacts appearing as a derivative shape along diagonal. These results are in excellent agreement with our own fs transient absorption (TA) spectra reported in the supplementary material (Fig. S2) and with previously published data by Kovalenko *et al.*[4]

The dynamical evolution of the HB2DES was quantitatively analyzed by 2D global fit, assuming sequential evolution through a series of first-order steps with increasing time constants τ_n (τ_{n+1} > τ_n), to yield a final spectrum that recovers back to the ground state with time constant τ_{fin}. The resulting 2D evolution-associated difference spectra (EADS) are reported in Fig. 3. Two components (1.2 and 4.2 ps) were needed to yield a good fit plus a fixed time long relaxation (τ_{fin} = 20 ps). The quality of the fit is shown by comparison of experimental points in the SE (red dots) and ESA (blue dots) regions vs fit (solid black), as shown in Figs. 3(d) and 3(e).

The first EADS in Fig. 3(a) reproduces the absorptive spectrum at T = 100 fs shown in Fig. 2. This component evolves in 1.2 ps to a second EADS, which shows attenuated, 400 cm^{-1} blueshifted ESA, quenched SE, and the formation of a weak hot ground state absorption feature centered at $\tilde{\nu}_3$ = 14 500 cm^{-1}. A fast internal conversion refilling the GS would quench the ESA and SE by the same amount, while here the ESA is weakly affected, but SE is fully relaxed. This component must then be due to the population evolving from the FC region of the S_1 potential toward a region with reduced S_1–S_0 transition dipole moment (TDM). Such amplitude variation is accompanied by the dynamic Stokes shift of the SE (which moves to the red of the spectral region probed by the WLC) indicating solvation. Thus, the disappearance of the SE feature is assigned to a decrease in both the SE TDM and the S_1–S_0 energy gap as a consequence of evolution on the ES PES, see Fig. 1(b). Such dynamics were previously rationalized on the basis of ps intramolecular electron transfer (iET) driven by an increase in ø and solvation. The present values are a factor of ≈2 longer than those recovered by Kovalenko *et al.*[4] The difference may reflect the different analysis methods and spectral ranges used to recover the iET time constants from TA and HB2DES methods.

The second component of 4.2 ps accounts for the quenching of the ESA extending from 17 000 to 22 000 cm^{-1} and simultaneous formation of a redshifted broad negative feature indicating product (HGS) absorption and revealing a GSB above the diagonal previously obscured by the strong ESA. The $\tilde{\nu}_3$ width of the GSB matches

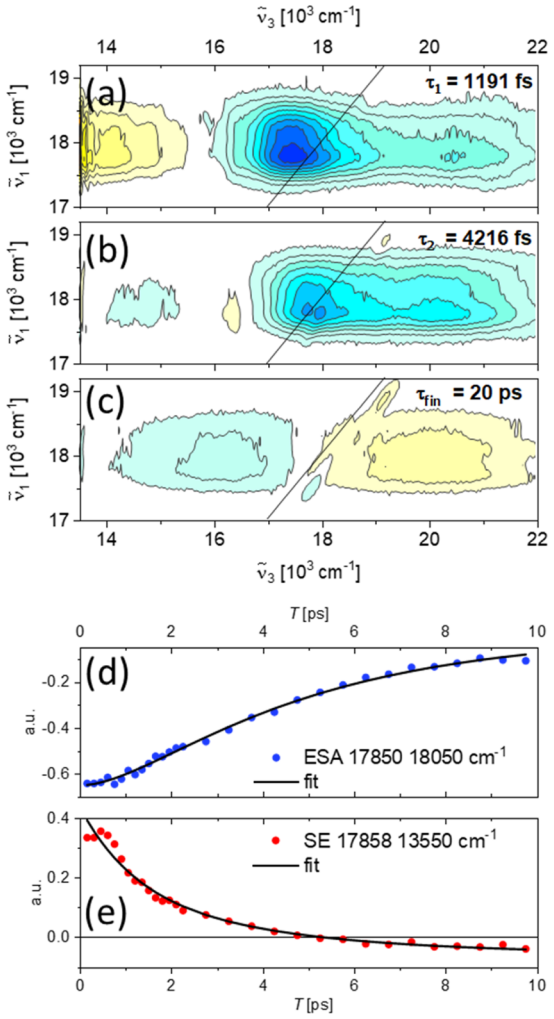

FIG. 3. (a)–(c) 2D EADS of B30 in EtOH excited at 18 000 cm^{-1}. (d) and (e) Experimental vs global fit traces at selected excitation-detection frequency pairs.

the high-energy side of the steady-state absorption, suggesting that spectral diffusion, i.e., resolvation of the GS occurs within a few ps from photoexcitation. The 4.2 ps component is assigned to back electron transfer (bET) populating the redshifted HGS. Kovalenko *et al.* reported a 4.8 ps ± 10% bET timescale in their TA study, in good agreement with the present results.[4]

TABLE I. iET, bET, and HGS VC timescales of B30 in EtOH and MeCN. The longest HGS cooling timescales were fixed.

	B30 in EtOH NOPA1	B30 in EtOH NOPA2	B30 in MeCN NOPA2
iET (ps)	1.2	0.89	0.09
bET (ps)	4.2	3.5	1.2
HGS cooling (ps)	20	20	7

Finally, the longest component accounts for VC of the HGS and was fixed at 20 ps, based on Reid and Barbara[3] who reported a ≈15 ps VC time and Duvanel *et al.* who reported biphasic VC with rates of 5 and 50 ps. The relaxation timescales for B30 in EtOH excited by NOPA 1 are summarized in Table I.

HB2DES of B30 in EtOH, NOPA2

Evolution of 2D absorptive spectra following photoexcitation on the red edge of the absorption spectrum of B30 in EtOH (centered at 16 200 cm^{-1}, Fig. 1) for T values between 0.1 and 0.85 ps is shown in Fig. 4, with more detail shown in Fig. S3. The earliest spectrum at T = 100 fs shows a broad positive feature between 13 500 and 16 000 cm^{-1} and broad negative ESA peaked at $\tilde{\nu}_3$ = 17 600 cm^{-1} and extending to >22 000 cm^{-1}. The ESA shoulder at 20 500 cm^{-1} observed upon excitation at 18 000 cm^{-1} is not present, suggesting different regions of the S_1 potential being populated, yielding distinct S_1–S_n ESA bands (see Figs. S2 and S5 for a direct comparison). When exciting at 16 200 cm^{-1}, the signal amplitude is a factor of two weaker than when exciting at the band maximum, resulting in correspondingly weaker nonlinear signals. Hence, the "tail" of the coherent artifact at T = 0 fs is comparable in amplitude with the resonant B30 response and distorts the shape of the absorptive HB2DES at T = 100 fs.

Over the first ps, the ESA peaked at 17 500 cm^{-1} exhibits a minor decay. The ~1 ps ≈ 400 cm^{-1} ESA blueshift observed after photoexcitation with NOPA1 does not appear upon NOPA2 excitation. Furthermore, over the first ps, the broad weak positive feature spanning $\tilde{\nu}_3$ = 13 500–16 000 cm^{-1} "splits" into two peaks whose gap along $\tilde{\nu}_3$ increases as a function of T as the "red side" redshifts, resulting in the formation of a fully resolved below diagonal peak at 16 000 cm^{-1}. Based on the steady-state absorption spectrum in MeCN and on the dynamics recovered with 18 000 cm^{-1} excitation, we assign the shifting and static positive features to SE and GSB, respectively [highlighted by arrows in Fig. 4(a)]. It is worth noting that the GSB feature (which is not observed on this timescale in the HB2DES for NOPA1, see Figs. 2 and 3) is much narrower than the steady-state absorption of B30 [Fig. 1(a)]. This suggests spectral hole burning in the inhomogeneously broadened ground state of B30 in EtOH, in agreement with previous studies.[1,31]

The spectral evolution between 1 and 10 ps is reported in the supplementary material (Fig. S3) and the 2D EADS are shown in Fig. S4 and their evolution resembles the 18 000 cm^{-1} pump data. Significantly, the recovered iET and bET rates are faster when exciting on the red side of the absorption spectrum (0.9 vs 1.2 ps for iET and 3.5 vs 4.2 ps for bET), as shown by the comparison of fit traces in Figs. 4(b) and 4(c) and from Table I. We propose that the small but reproducible increase in the iET rate observed upon red-edge excitation of the B30 absorption arises from the photoexcitation of distinct conformational subsets of the inhomogeneously broadened GS. NOPA2 pulses [Fig. 1(a)] excite a population that has a larger dihedral angle between the phenolate and pyridinium rings than that excited by NOPA1 pulses [Fig. 1(b)]. The "pre-twisted" ES population created by NOPA2 can then reach the iET region of S_1 (i.e., its minimum) more rapidly. This agrees with prior theoretical studies of Kharlanov and Rettig and Hogiu *et al.* who showed that the minimum of the S_1 potential is reached via an increase in the angle between the phenolate donor and pyridinium acceptor moieties of

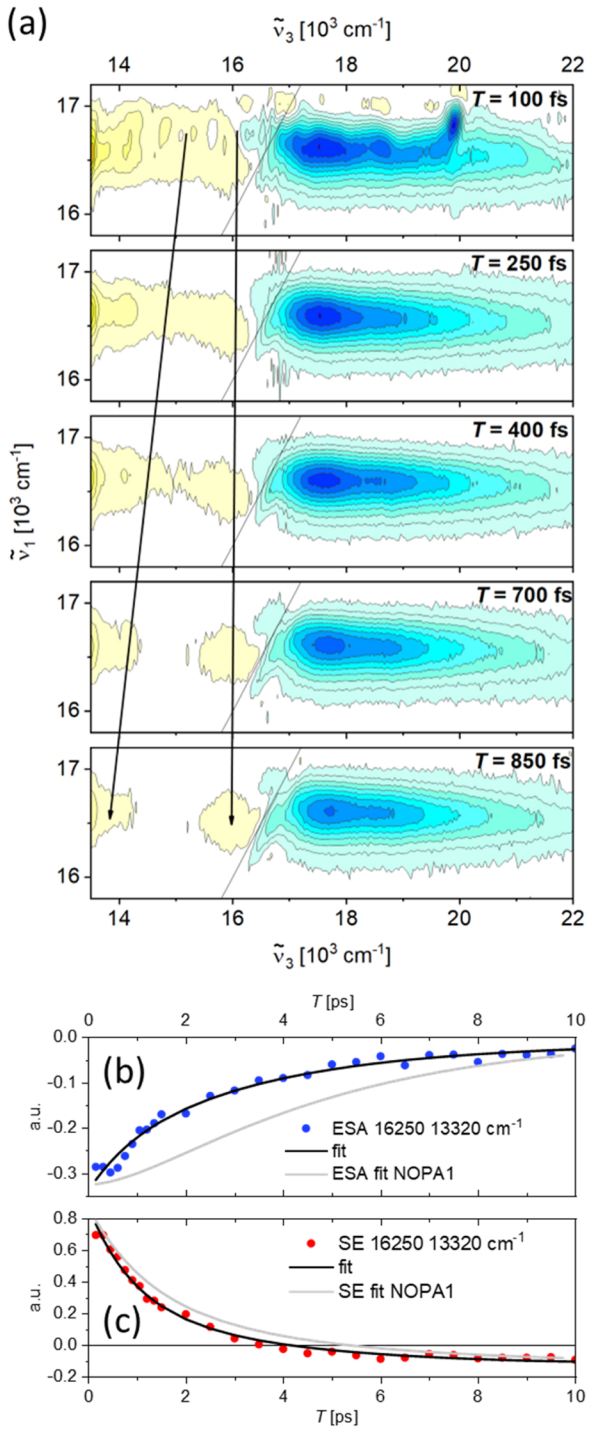

FIG. 4. (a) Absorptive HB2DES spectra of B30 in EtOH after excitation at 16 200 cm^{-1} at selected waiting time points between 0.1 and 0.85 ps. The intensity is given by 21 contour lines; positive signals are shown in yellow, and negative signals are shown in blue. All spectra are normalized to the negative ESA amplitude at T = 0.1 ps. (b) and (c) Experimental and global fit traces at selected excitation-detection frequency pairs. Fit data for 18 000 cm^{-1} excitation are shown in gray for comparison.

B30 (or simpler model compounds).[33,35] Downhill evolution on the S_1 potential following higher energy (NOPA1) excitation is reflected in the blueshift of the ESA. Conversely, after NOPA2 excitation, no such blue shift is observed, suggesting that the redshifted excitation pulse pair directly populates a region of the S_1 PES close to its minimum, in agreement with our computational results [Fig. 1(b)].

On the few ps timescale, the persistence of long-lived distinct species is shown in Fig. S5, highlighting the differences between the $\tilde{\nu}_1$ integrals of the HB2DES obtained upon excitation at 16 200 and 18 000 cm^{-1}. We propose that such sub-populations are due to different H-bond networks, which undergo bET at different rates, as shown by the slower bET rate measured upon red-edge excitation. A role of H-bonding on the bET kinetics was demonstrated through isotope effects and modeling by Barbara *et al.*[3]

HB2DES of B30 in MeCN, NOPA2

In this case, NOPA2 excites B30 near the peak of the absorption spectrum, so the data should be compared to NOPA1 in EtOH, although MeCN does not form H-bonds with B30. The absorptive HB2DES between 0.1 and 0.85 ps of B30 in MeCN are reported in Fig. 5(a). The time-dependent amplitudes of the ESA and GSB are shown for T between 1 and 10 ps in Figs. 5(b) and 5(c) respectively, while the HB2DES at T > 1 ps are shown in the supplementary material (Fig. S6) and show full recovery of the HGS and GSB within 10 ps. The spectrum at T = 100 fs shows positive GSB peaked ≈300 cm^{-1} to the red of the diagonal and extending to 14 000 cm^{-1}, and a broad negative ESA extending from 17 000 cm^{-1} toward the high energy edge of the WLC probe, with a peak at 19 300 cm^{-1}. The lack of positive SE at the earliest waiting times indicates that the emissive excited state is being quenched on a sub-100 fs timescale, in agreement with the reported iET rate in the MeCN solvent.[4] The broader GSB in MeCN compared to EtOH suggests that the GS of B30 is more homogeneous in this nonprotic solvent, in agreement with Lobaugh and Rossky.[36] The contrast with the inhomogeneous broadening observed in ethanol suggests that the different conformers of B30 persist longer due to the slower dynamics and distinct H-bond geometries in the protic solvent.

Over the first ps, the ESA amplitude decays by >50% and blueshifts by ≈600 cm^{-1}, as highlighted by the arrow in Fig. 5(a). Such ESA evolution is accompanied by asymmetrical narrowing of the GSB band because of the formation of a positive HGS absorption, which cannot be fully resolved as it is centered in the near-infrared near-infrared is correct (NIR) (although a weak poorly resolved negative feature appears close to the red edge of $\tilde{\nu}_3$ at ≈13 600 cm^{-1}). At 3.5 ps, the ESA has fully decayed as the red-NIR-absorbing HGS is formed, as revealed by the incomplete recovery of the GSB between 16 000 and 20 000 cm^{-1} (Fig. S6). The HGS relaxation is complete within less than 10 ps, as shown by traces in Figs. 5(b) and 5(c).

The 2D EADS for NOPA2 excitation in MeCN is shown in Fig. S7. The initial spectrum shows weak positive GSB+SE and a strong broad negative ESA band on the red and blue energy sides of the diagonal, respectively; the line shape is perturbed by the nonresonant response at T = 0 fs. The component formed in 90 fs, which we take as an upper limit for iET in MeCN, shows an ESA blueshift causing an apparent rise time of the GSB [see trace in Fig. 5(c)] and quenching of the positive SE feature. The timescale of this component agrees with the solvation time of MeCN suggesting iET being

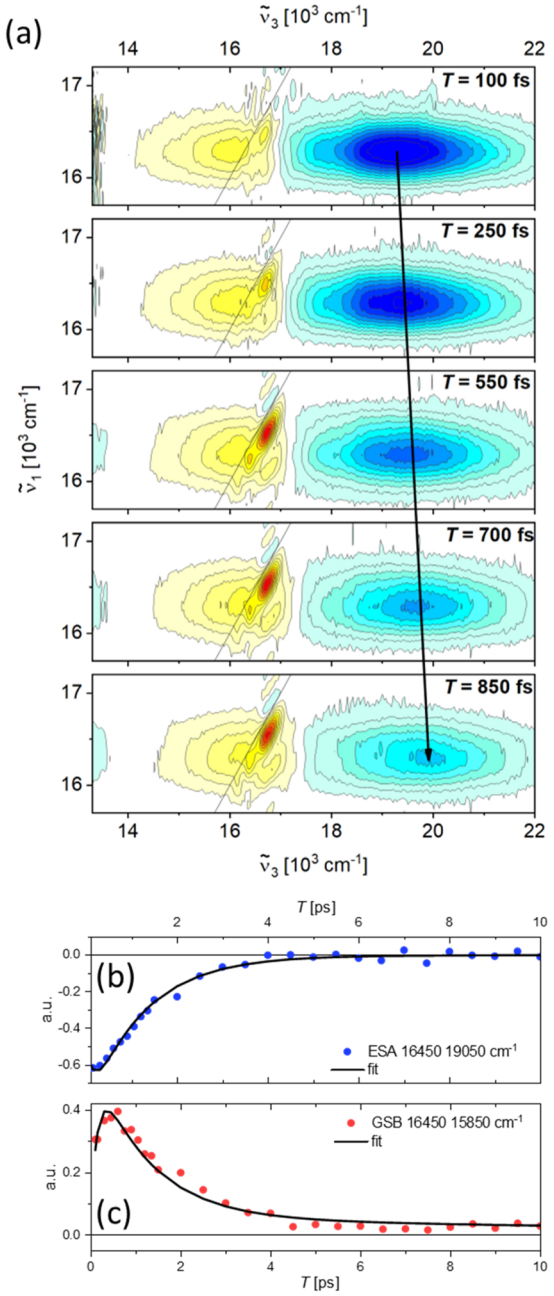

FIG. 5. (a) Absorptive HB2DES spectra of B30 in MeCN after excitation at 16 200 cm^{-1} at selected waiting time points between 0.1 and 0.85 ps. The intensity is given by 21 contour lines; positive signals are shown in yellow, and negative signals are shown in blue. All spectra are normalized to the negative ESA amplitude at T = 0.1 ps. (b) and (c) Experimental vs global fit traces at selected excitation-detection frequency pairs.

controlled by solvation dynamics,[34] in agreement with Kovalenko *et al.*[4] The sub-100 fs iET is followed by bET populating the hot ground state with a 1.2 ps timescale, as shown by the residual bleach centered at 18 000 cm^{-1}, which refills in <10 ps (τ_{fin} was fixed to 7 ps). The dynamics in MeCN are overall faster than in alcohols, in agreement with previously published fsTA data on B30 in MeCN.[4] The timescales of iET, bET, and VC of the HGS of B30 in EtOH (with NOPA1 and NOPA2) and MeCN (NOPA2) are summarized in Table I. The fast iET in MeCN is consistent with solvent control. The mean solvation time measured for MeCN is 260 fs, while the fastest (librational) component is 120 fs.[34] Comparison with the 90 fs iET suggests that the librational solvent response alone is sufficient to stabilize electron transfer of B30 in MeCN. The iET time in ethanol is on the time scale of the librational relaxation plus fastest exponential relaxation in the solvation time, 1.4 ps.[34] The influence of the post librational relaxation in ethanol may reflect solvent molecules rearranging within the H-bond network around B30, which can apparently influence the iET rate. In either solvent, the present data are consistent with the rate of iET being under control of solvation dynamics, as previously concluded.[4,5] The bET is also slower than the mean solvation times for MeCN but faster than for EtOH. The rate of bET is determined by access to the conical intersection between excited and ground state, which involves intermolecular reorganization and solvation. The slower access to the conical intersection in EtOH likely reflects the slower dynamics and H-bond interaction, which were noted above to lead to longer lived (hence inhomogeneous) conformations of B30.

Vibrational wavepacket dynamics

On the basis of the sub-ps/ps iET/bET reaction rates in B30, a role for molecular vibrations in its excited-state dynamics was proposed by several groups.[2,4,5,7] To investigate this through HB2DES, vibrationally coherent dynamics in B30 in EtOH excited at 18 200 cm^{-1} and in MeCN excited at 16 200 cm^{-1} were measured. The waiting time T was scanned in 15 fs steps between 0 and 1800 fs to resolve ground and excited state vibrational frequencies and so create "beatmaps" of low frequency resonance Raman active molecular vibrations. Beatmaps are a full frequency domain picture in which the contribution due to a specific Raman mode is resolved as a function of excitation ($\tilde{\nu}_1$) and detection ($\tilde{\nu}_3$) dimensions of the 2D spectrum and with respect to its beat frequency and phase over T. Beatmaps are obtained by a procedure previously discussed in the literature and outlined in the supplementary material (Fig. S8).[19,37,38] Our experimental implementation of HB2DES separates the real and imaginary parts of the rephasing (photon-echo) and nonrephasing (free induction decay) contributions to the 2DES signal, allowing us to uniquely assign ground vs excited state vibrational coherence. This is especially relevant when coherent dynamics are superimposed on broad, overlapping, and dynamically shifting electronic features, as for B30. This distinguishes HB2DES from the 2-pulse impulsive Raman methods, which initiate ground and excited state wavepacket dynamics via a pair of non-time ordered pump field–matter interactions with identical wavevectors, leading to ambiguity in discrimination of wavepackets sampling the S_1 or the S_0 PESs. In the following, we focus on rephasing signals that report on vibrational modes active in the S_0 (positive frequencies) and S_1 (positive and negative frequencies) PESs. Selection of the relevant vibrational wavenumbers for beatmap analysis is done by inspecting the rephasing vibrational (summary Raman) spectra shown in Figs. 6(a) and 6(b), which are obtained by integration of the 3D spectrum over $\tilde{\nu}_1$ and $\tilde{\nu}_3$ as previously described.[19,37] The

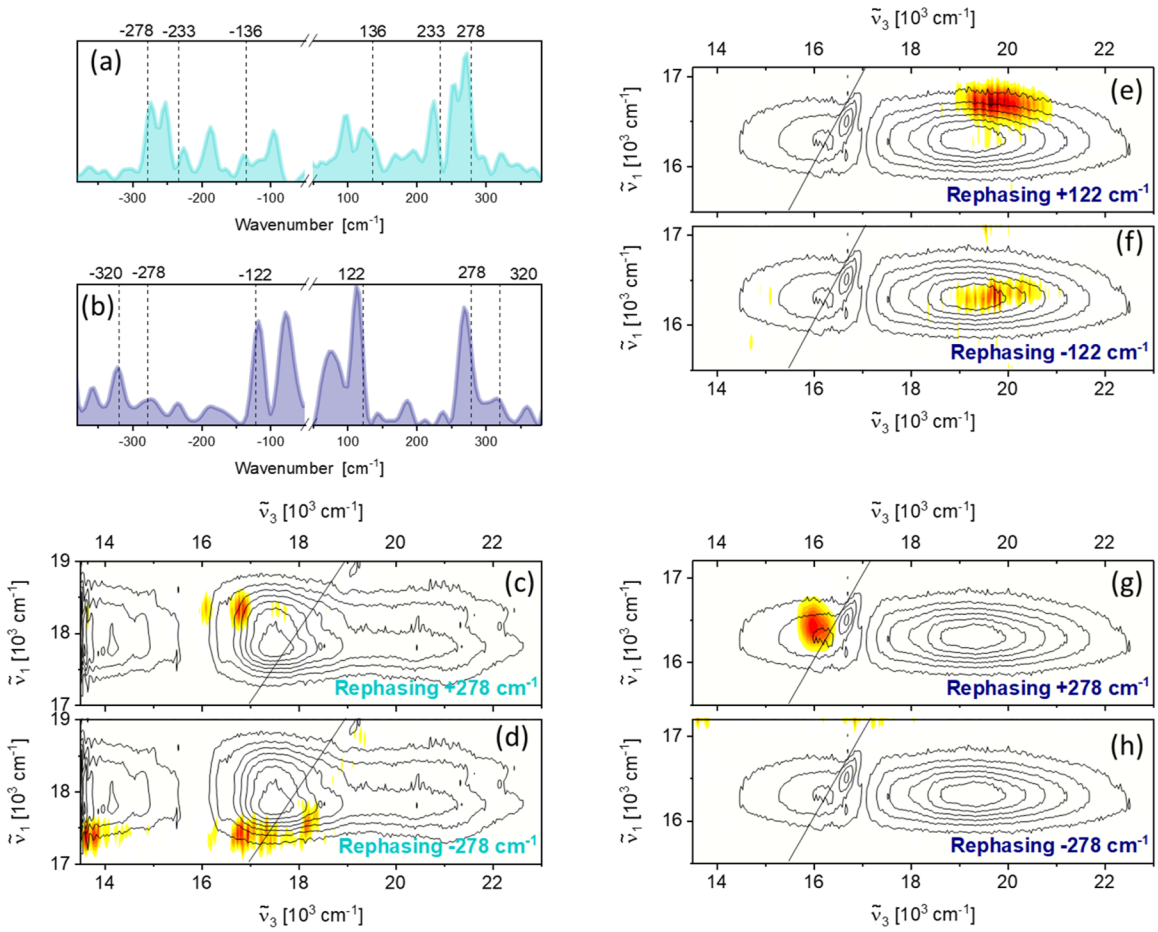

FIG. 6. (a) Integrated rephasing vibrational spectrum (summary Raman) of B30 in EtOH after impulsive excitation centered at 18 200 cm^{-1}. Positive frequencies report on ground and excited state vibrational coherence while negative frequencies are solely due to excited state vibrational coherences. Panel (b) is the same as panel (a) for MeCN excited at 16 200 cm^{-1}. (c) and (d) Rephasing beatmaps of the positive and negative rephasing 278 cm^{-1} mode in EtOH are shown as white–yellow–red heat maps and amplitude normalized to 1. The contours show the absorptive HB2D spectrum at $T = 0.15$ ps. Panels (e) and (f) are the same as panels (c) and (d) for the 122 cm^{-1} vibration of B30 in MeCN excited at 16 200 cm^{-1}. Panels (g) and (h) are the same as panels (e) and (f) for the 278 cm^{-1} vibration.

characterization of signal to noise and signal above background in beatmaps is described in the supplementary material, Figs. S10 and S11.

The rephasing "summary Raman" of B30 in EtOH [Fig. 6(a)] agrees with the spontaneous, impulsive, and stimulated Raman experiments on B30 in short-chain alcohols by McHale, Rafiq, and Frontiera[2,5,39] and propylene carbonate by Hogiu *et al.*[35] These authors assigned the strong modes in the 100–400 cm^{-1} region to torsion or out-of-plane (OOP) bending between the central phenolic and pyridine rings. The strong mode at 290 cm^{-1} (which we observe at 278 cm^{-1}) is assigned by Hogiu *et al.* for inversion of the pyridinic N.[35] The modes at 136 (torsion), 233 (OOP bending), and 278 cm^{-1} (N inversion) are all contributing to the negative side of the vibrational spectrum in Fig. 6(a), hence they are active in the S_1 PES.[37,40] Although, as these modes are observed to contribute more strongly on the positive Raman frequency side (reporting on both S_1 and S_0 coherences), we conclude that ground state wavepackets are also contributing to the coherent response.

The amplitude ratio between positive and negative peaks for a given mode frequency, assuming similar displacements (hence Franck–Condon factors) for the S_0–S_1 and S_1–S_n transitions, scales as the sum of Liouville-space pathways involving positive/negative, i.e. $(S_0 + S_1)/S_1$ coherence.[37,38,41] This ratio is close to ≈2/1 for the 136, 233, and 278 cm^{-1} modes.[41] This is the ratio predicted by using the displaced harmonic oscillator (DHO) model.[42,43] The Raman active frequencies discussed above are well-reproduced in the calculated off-resonance S_0 Raman spectrum of B30 in vacuum, as shown in Fig. S9 (supplementary material). The intensity differences between the calculated and experimental Raman signals could stem from either anharmonicity, which is of particular relevance for low frequency vibrations, or electronic resonance enhancement factors, which are not accounted for in the calculation.

The rephasing beatmaps of the most intense mode at ± 278 cm^{-1} (N inversion) in EtOH are shown in Figs. 6(c) and 6(d). Their amplitude distribution agrees with the DHO model, which predicts the positive beatmap amplitude being centered, along $\tilde{\nu}_1$, (at least) one vibrational quantum to the blue of the negative beatmap. This is a consequence of the density matrices $|s_0\rangle\langle s_1|$ or $|s_1\rangle\langle s_0|$ corresponding to positive or negative frequencies, respectively (where *s* is an arbitrary electronic state and subscripts indicate quanta of an arbitrary vibrational mode). Comparison with the absorptive data (black contours) shows that the main contribution is localized in the ESA region, but for the positive beatmap, we cannot rule out S_0 contributions from an overlapping GSB. Furthermore, the negative frequency beatmap shows weak coherent vibrational response at $\tilde{\nu}_3 \leq 14\,000$ cm^{-1} where the dynamically redshifting SE contributes.

The linewidth, i.e., the vibrational dephasing lifetime of the modes contributing to the negative side (i.e., S_1 active) of the rephasing integrated vibrational spectrum are comparable with signals originating from wavepackets evolving on "nonreactive" PESs, as in molecular dyes such as cresyl violet.[37] On the basis of the linewidths and of the relative positive/negative amplitudes of the integrated vibrational response, we can rule out any role of the Raman active N inversion mode in promoting the iET in EtOH. This interpretation is supported by its beatmaps (±278 cm^{-1}) being consistent with what is predicted by the DHO model. This conclusion is not surprising as the fastest population component measured for B30 in EtOH and assigned to iET is 1.2 ps, comparable with typical vibrational dephasing times of organic dyes.

The integrated low frequency vibrational response of B30 in MeCN is shown in Fig. 6(b). It is mostly in agreement with the integrated Raman measured in EtOH and impulsive stimulated Raman data reported by Rafiq *et al.* in the same solvent.[5] The strong torsional mode at 122 cm^{-1}, observed at 136 cm^{-1} in EtOH, contributes to both the negative and positive sides of the summary Raman in Fig. 6(b), as expected for a S_1 active mode. Although, as the difference in amplitude between the negative (ES) and the positive (GS + ES) peaks is small, we can conclude that it is only weakly active in the ground state, possibly because of the smaller S_0–S_1 displacements along this normal mode in MeCN vs EtOH or of the different electronic resonance enhancement effects in the two solvents, arising from the previously discussed solvent-dependent absorptive spectra. We propose that the 10 cm^{-1} redshift of this torsion from EtOH to MeCN solvents is due to the lack of H-bonding in the latter. Furthermore, a strong signal assigned to N inversion is present in MeCN at +278 cm^{-1}, the same frequency as in EtOH.

The rephasing beatmaps of the ± 122 cm^{-1} mode in MeCN are reported in Figs. 6(e) and 6(f). Along $\tilde{\nu}_3$, the amplitude is localized on the strong ESA feature (see contours) as expected for S_1 coherences contributing to the rephasing positive ESA pathways. Conversely, the lack of signals below the diagonal GSB region suggests weak GS activity of such vibration, i.e., a negligible S_0–S_1 displacement. However, for a rigorously null displacement between the S_0 and S_1 PESs, the pump pulses could not prepare a superposition of vibrational states in S_1 which then modulates the S_1–S_n ESA. Thus, we speculate that along this coordinate, the S_0–S_1 displacement is too weak to give rise to an appreciable signal in the GSB region (whose amplitude depends on the fourth power of the FC integral between the S_0 and S_1 PESs) but large enough to initiate the wavepacket motion modulating the ESA signal during *T*, whose oscillatory amplitude is dictated by the product of the squares of the FC integrals for the S_0–S_1 and the S_1–S_n PESs. We can thus conclude that the 122 cm^{-1} torsion is considerably displaced between the S_1 and S_n potentials.[37]

The shape and location of the +122 cm^{-1} beatmap in MeCN can be rationalized by a 3-level displaced harmonic oscillator (DHO) model, considering the vibrational levels $v = 0, 1, 2$ of each electronic PES, and where the S_1–S_n energy gap is larger than the S_0–S_1 energy gap, causing the ESA to appear above the diagonal. This situation resembles the case of the model dye cresyl violet, whose beatmaps for excited state absorption we previously discussed in detail.[37] In brief, impulsive excitation of resonance Raman active modes coupled to an electronic transition drive wavepacket motion during the waiting time, and thus beatmap amplitude at specific points on the excitation/detection frequency plane, whose $(\tilde{\nu}_1; \tilde{\nu}_3)$ coordinates are determined by double-sided Feynman diagrams (DSFDs). Typical widths of such features are a few hundred cm^{-1} and not correlated to the bandwidth of the underlying electronic transition. In the present case of low frequency vibrations, pump pulses can resonantly excite multiple vibrational quanta above the 0-0 $S_n \leftarrow S_1$ transition, increasing the total number of DSFDs contributing to the coherent response. Such signals, at room temperature (RT), rather than being detected as isolated peaks coalesce into broader features centered between the point amplitudes predicted by individual DSFDs. As for the amplitude distribution along the detection axis $\tilde{\nu}_3$, the beatmap is localized close to the maximum of the broad ESA spectrum. Vibronic transitions to highly excited vibrational quanta within the S_n manifold (which would appear blueshifted from the ESA center at ≈19 500 cm^{-1} by integer multiples of 122 cm^{-1}), despite being resonant with the broad spectrum of the continuum probe, have negligibly small FC integrals, hence do not contribute to the measured vibrationally coherent response.

The −122 cm^{-1} rephasing beatmap shows amplitude located on the ESA feature but at lower $\tilde{\nu}_1$, in line with the DHO model predictions. Furthermore, as the mode frequency is comparable with kT, several vibrational levels in the S_0 PES above $|g_0\rangle\langle g_0|$ will be populated at room temperature. This increases the total number of available (degenerate) Liouville-space pathways, such that no specific vibrational coherence pathway is resolved. The amplitude distribution observed for the rephasing ±122 cm^{-1} beatmaps is thus fully explained by the DHO model, suggesting that this vibrational coordinate is not coupled to the iET reaction coordinate, despite its large displacement.

A distinctive feature of the integrated vibrational spectrum of B30 in MeCN [Fig. 6(b)] is the quenched signal at −278 cm^{-1}, which is barely distinguishable from the baseline. This behavior contrasts sharply with the predictions of the DHO model. For a mode active in both S_0 and S_1 (as observed in EtOH) the DHO model anticipates an amplitude at −278 cm^{-1} that is only a factor of two smaller than that at +278 cm^{-1}. This lack of amplitude at −278 cm^{-1} implies that while this normal mode is strongly contributing to the GS coherent response, it is barely active in the ES PES. Such an effect could arise from a negligible displacement between the S_1 and S_n PESs in MeCN. Alternatively, if the excited state 278 cm^{-1} vibration (125 fs period) was active along the iET coordinate, its wavepacket will be rapidly dephased due to the sub-100 fs iET. Interestingly, the deviation from the relative positive/negative amplitude ratio predicted by using the DHO model seems to be unique to the N inversion mode

at 278 cm^{-1}, as the strong excited state torsion at −122 cm^{-1} does not show such behavior. The latter is hence a spectator mode of the iET, orthogonal to the reaction coordinate. The linewidth of all resonance Raman active modes of B30 in MeCN are slightly broader than in EtOH [compare Figs. 6(a) and 6(b)]. A correlation between vibrational dephasing and bET times (4.2 and 1.2 ps in EtOH and MeCN) was previously reported by Rafiq *et al.*[5]

The beatmaps of the intense ±278 cm^{-1} mode in MeCN are reported in Figs. 6(g) and 6(h). The positive beatmap amplitude is centered at $\tilde{\nu}_1$ = 16 500 cm^{-1} in the high wavenumber region of the GSB feature as indicated by the contours, while the ESA region and negative beatmap do not show any signal above the noise floor. The lack of signals in the ESA region of the +278 cm^{-1} and in the −278 cm^{-1} beatmaps indicates that this mode, in the MeCN solvent, is only active in S_0. As this mode is strongly contributing to the excited state coherent response of B30 in EtOH, in which the iET reaction takes place on a ps timescale, while it is only GS active in MeCN where iET occurs with a sub-100 fs rate, we propose that this inversion mode is dephased rapidly due to iET, hence it is coupled to the intramolecular electron transfer reaction coordinate.

In summary, wavepacket analysis of beatmaps revealed solvent-dependent GS/ES relative amplitude variations for the low frequency resonance Raman active vibrations and a solvent-dependent frequency shift. These differences are assigned to H-bonding effects, different displacements, and resonance enhancements given by different electronic states. Furthermore, it showed that in EtOH, the N inversion at 278 cm^{-1} contributes significantly to the ES coherence, while it is only active in the ground state in MeCN. That the iET rate is more than an order of magnitude slower in EtOH (1.2 ps) than in MeCN (≈90 fs), and the latter is below the vibrational period of the 278 cm^{-1} mode (125 fs) suggests that such N inversion is active along the iET coordinate in MeCN, hence damped within its first oscillation period by the sub-100 fs iET.

CONCLUSIONS

The ultrafast photoinduced dynamics of B30 were studied by HB2DES in polar protic EtOH and polar nonprotic MeCN. The results agree with previously reported fsTA data and are discussed based on the four-level scheme proposed by Kovalenko *et al.*[4] involving sequential iET and bET (IC), followed by vibrational cooling of the HGS. Tuning the pump wavelength across the steady-state absorption of B30 in EtOH revealed an effect of multiple conformers and H-bonding in the inhomogeneously broadened GS on the measured iET and bET rates. Such dependences are assigned to selective excitation of twisted vs planar B30 conformers and to H-bonded structures frozen within the B30 "photocycle" and were supported by quantum chemical calculations. In a study of vibrational coherence dynamics, the complex-valued HB2DES data allowed us to uniquely assign ground vs excited state low frequency vibrational coherences. Beatmaps of selected modes of B30 in EtOH and MeCN were reported and discussed. On the basis of the solvent-induced differences on the vibrationally coherent response of B30, it was proposed that while the ≈1 ps iET in EtOH is not affected by excited state wavepacket motion, the N inversion coordinate is coupled to the sub-100 fs iET measured in MeCN, leading to rapid dephasing within a vibrational period.

SUPPLEMENTARY MATERIAL

The supplementary material encompasses additional fsTA and HB2DES data and 2DEADS, beatmap calculation procedure, calculated off-resonance S_0 Raman spectrum of B30, beatmap SNR and noise floor characterization, and B30 coordinates.

ACKNOWLEDGMENTS

The simulations presented in this article were conducted on the High-Performance Computing Cluster supported by the Research and Specialist Computing Support service at the University of East Anglia. We acknowledge support from the Engineering and Physical Sciences Research Council under Award Nos. EP/V00817X/1 to S.R.M. and EP/W018691 to J.N.B. G.B. acknowledges the Leverhulme Trust for funding him through an Early Career Fellowship (Grant No. ECF-2023-195).

AUTHOR DECLARATIONS

Conflict of Interest

The authors have no conflicts to disclose.

Author Contributions

Stephen R. Meech: Conceptualization (equal); Funding acquisition (equal); Methodology (equal); Writing – review & editing (equal). **James N. Bull**: Data curation (equal); Formal analysis (equal); Writing – review & editing (equal). **Giovanni Bressan**: Conceptualization (equal); Data curation (equal); Formal analysis (equal); Investigation (equal); Methodology (equal); Project administration (equal); Writing – original draft (equal); Writing – review & editing (equal).

DATA AVAILABILITY

The data that support the findings of this study are available from the corresponding author upon reasonable request.

REFERENCES

[1] R. Pandian, H. Burda, I. Alfurayj, C. Reichardt, and C. Burda, "60 years of Betaine 30–From solvatochromic discovery to future Frontiers," J. Phys. Chem. B **128**(29), 6990–7001 (2024).

[2] W. Ruchira Silva and R. R. Frontiera, "Excited state structural evolution during charge-transfer reactions in betaine-30," Phys. Chem. Chem. Phys. **18**(30), 20290–20297 (2016).

[3] P. J. Reid and P. F. Barbara, "Dynamic solvent effect on betaine-30 electron-transfer kinetics in alcohols," J. Phys. Chem. **99**(11), 3554–3565 (1995).

[4] S. A. Kovalenko, N. Eilers-König, T. A. Senyushkina, and N. P. Ernsting, "Charge transfer and solvation of betaine-30 in polar solvents - A femtosecond broadband transient absorption study," J. Phys. Chem. A **105**(20), 4834–4843 (2001).

[5] S. Rafiq and G. D. Scholes, "Is back-electron transfer process in Betaine-30 coherent?," Chem. Phys. Lett. **683**, 500–506 (2017).

[6] G. Duvanel, J. Grilj, H. Chaumeil, P. Jacques, and E. Vauthey, "Ultrafast excited-state dynamics of a series of zwitterionic pyridinium phenoxides with increasing sterical hindering," Photochem. Photobiol. Sci. **9**(7), 908–915 (2010).

[7]G. C. Walker, E. Aakesson, A. E. Johnson, N. E. Levinger, and P. F. Barbara, "Interplay of solvent motion and vibrational excitation in electron-transfer kinetics: Experiment and theory," J. Phys. Chem. **96**(9), 3728–3736 (1992).
[8]P. F. Barbara, T. J. Meyer, and M. A. Ratner, "Contemporary issues in electron transfer research," J. Phys. Chem. **100**(31), 13148–13168 (1996).
[9]T. Kumpulainen, B. Lang, A. Rosspeintner, and E. Vauthey, "Ultrafast elementary photochemical processes of organic molecules in liquid solution," Chem. Rev. **117**(16), 10826–10939 (2017).
[10]J. D. Hybl, A. W. Albrecht, S. M. G. Faeder, and D. M. Jonas, "Two-dimensional electronic spectroscopy," Chem. Phys. Lett. **297**, 307 (1998).
[11]A. Gelzinis, R. Augulis, V. Butkus, B. Robert, and L. Valkunas, "Two-dimensional spectroscopy for non-specialists," Biochim. Biophys. Acta, Bioenerg. **1860**(4), 271–285 (2019).
[12]E. Fresch, F. V. A. Camargo, Q. Shen, C. C. Bellora, T. Pullerits, G. S. Engel, G. Cerullo, and E. Collini, "Two-dimensional electronic spectroscopy," Nat. Rev. Methods Primers **3**(1), 84 (2023).
[13]S. Biswas, J. Kim, X. Zhang, and G. D. Scholes, "Coherent two-dimensional and broadband electronic spectroscopies," Chem. Rev. **122**(3), 4257–4321 (2022).
[14]N. S. Ginsberg, Y. C. Cheng, and G. R. Fleming, "Two-dimensional electronic spectroscopy of molecular aggregates," Acc. Chem. Res. **42**(9), 1352–1363 (2009).
[15]F. D. Fuller and J. P. Ogilvie, "Experimental implementations of two-dimensional Fourier transform electronic spectroscopy," Annu. Rev. Phys. Chem. **66**(1), 667–690 (2015).
[16]J. Dostál, T. Mančal, R.-n. Augulis, F. Vácha, J. Pšenčík, and D. Zigmantas, "Two-dimensional electronic spectroscopy reveals ultrafast energy diffusion in chlorosomes," J. Am. Chem. Soc. **134**(28), 11611–11617 (2012).
[17]G. Bressan, S. E. Penty, D. Green, I. A. Heisler, G. A. Jones, T. A. Barendt, and S. R. Meech, "Ultrafast and coherent dynamics in a solvent switchable 'pink box' perylene diimide dimer," Angew. Chem., Int. Ed. Engl. **136**, e202407242 (2024).
[18]G. Bressan, I. Chambrier, A. N. Cammidge, and S. R. Meech, "Symmetry-breaking charge-separation in a subphthalocyanine dimer resolved by two-dimensional electronic spectroscopy," J. Phys. Chem. C **129**(2), 1069–1077 (2025).
[19]G. Bressan, I. A. Heisler, G. M. Greetham, A. Edmeades, and S. R. Meech, "Half-broadband two-dimensional electronic spectroscopy with active noise reduction," Opt. Express **31**(25), 42687 (2023).
[20]P. F. Tekavec, J. A. Myers, K. L. M. Lewis, and J. P. Ogilvie, "Two-dimensional electronic spectroscopy with a continuum probe," Opt. Lett. **34**(9), 1390 (2009).
[21]P. A. Tekavec, K. L. M. Lewis, F. D. Fuller, J. A. Myers, and J. P. Ogilvie, "Toward broad bandwidth 2-d electronic spectroscopy: Correction of chirp from a continuum probe," IEEE J. Sel. Top. Quantum Electron. **18**(1), 210–217 (2012).
[22]Z. Zhang, K. L. Wells, E. W. J. Hyland, and H.-S. Tan, "Phase-cycling schemes for pump–probe beam geometry two-dimensional electronic spectroscopy," Chem. Phys. Lett. **550**, 156–161 (2012).
[23]Y. Feng, I. Vinogradov, and N.-H. Ge, "General noise suppression scheme with reference detection in heterodyne nonlinear spectroscopy," Opt. Express **25**(21), 26262 (2017).
[24]C. Bannwarth, S. Ehlert, and S. Grimme, "GFN2-xTB—An accurate and broadly parametrized self-consistent tight-binding quantum chemical method with multipole electrostatics and density-dependent dispersion contributions," J. Chem. Theory Comput. **15**(3), 1652–1671 (2019).
[25]S. Lee, M. Filatov, S. Lee, and C. H. Choi, "Eliminating spin-contamination of spin-flip time dependent density functional theory within linear response formalism by the use of zeroth-order mixed-reference (MR) reduced density matrix," J. Chem. Phys. **149**(10), 104101 (2018).
[26]F. Neese, F. Wennmohs, U. Becker, and C. Riplinger, "The ORCA quantum chemistry program package," J. Chem. Phys. **152**(22), 224108 (2020).
[27]M. W. Schmidt, K. K. Baldridge, J. A. Boatz, S. T. Elbert, M. S. Gordon, J. H. Jensen, S. Koseki, N. Matsunaga, K. A. Nguyen, S. Su, T. L. Windus, M. Dupuis, and J. A. Montgomery, "General atomic and molecular electronic structure system," J. Comput. Chem. **14**(11), 1347–1363 (1993).
[28]T. H. Dunning, "Gaussian basis sets for use in correlated molecular calculations. I. The atoms boron through neon and hydrogen," J. Chem. Phys. **90**(2), 1007–1023 (1989).
[29]A. D. Becke, "A new mixing of Hartree–Fock and local density-functional theories," J. Chem. Phys. **98**(2), 1372–1377 (1993).
[30]R. Sure and S. Grimme, "Corrected small basis set Hartree-Fock method for large systems," J. Comput. Chem. **34**(19), 1672–1685 (2013).
[31]X. Zhao, F. J. Knorr, and J. L. McHale, "Temperature-dependent absorption spectrum of betaine-30 in methanol," Chem. Phys. Lett. **356**(3–4), 214–220 (2002).
[32]Š. Budzák, T. Jaunet-Lahary, A. D. Laurent, C. Laurence, M. Medved', and D. Jacquemin, "Exploring the solvatochromism of betaine 30 with ab initio tools: From accurate gas-phase calculations to implicit and explicit solvation models," Chem. - Eur. J. **23**(17), 4108–4119 (2017).
[33]V. Kharlanov and W. Rettig, "Experimental and theoretical study of excited-state structure and relaxation processes of betaine-30 and of pyridinium model compounds," J. Phys. Chem. A **113**(40), 10693–10703 (2009).
[34]M. L. Horng, J. A. Gardecki, A. Papazyan, and M. Maroncelli, "Subpicosecond measurements of polar solvation dynamics: Coumarin 153 revisited," J. Phys. Chem. **99**(48), 17311–17337 (1995).
[35]S. Hogiu, J. Dreyer, M. Pfeiffer, K.-W. Brzezinka, and W. Werncke, "Vibrational analysis and excited-state geometric changes of betaine-30 derived from Raman and infrared spectra combined with *ab initio* calculations," J. Raman Spectrosc. **31**(8–9), 797–803 (2000).
[36]J. Lobaugh and P. J. Rossky, "Solvent and intramolecular effects on the absorption spectrum of betaine-30," J. Phys. Chem. A **104**(5), 899–907 (2000).
[37]G. Bressan, D. Green, G. A. Jones, I. A. Heisler, and S. R. Meech, "Two-dimensional electronic spectroscopy resolves relative excited-state displacements," J. Phys. Chem. Lett. **15**(10), 2876–2884 (2024).
[38]F. V. de A Camargo, L. Grimmelsmann, H. L. Anderson, S. R. Meech, and I. A. Heisler, "Resolving vibrational from electronic coherences in two-dimensional electronic spectroscopy: The role of the laser spectrum," Phys. Rev. Lett. **118**(3), 033001 (2017).
[39]X. Zhao, J. A. Burt, and J. L. McHale, "Resonance Raman analysis of nonlinear solvent dynamics: Betaine-30 in ethanol," J. Chem. Phys. **121**(22), 11195–11201 (2004).
[40]F. V. A. Camargo, H. L. Anderson, S. R. Meech, and I. A. Heisler, "Full characterization of vibrational coherence in a porphyrin chromophore by two-dimensional electronic spectroscopy," J. Phys. Chem. A **119**(1), 95–101 (2014).
[41]D. Green, G. Bressan, I. A. Heisler, S. R. Meech, and G. A. Jones, "Vibrational coherences in half-broadband 2D electronic spectroscopy: Spectral filtering to identify excited state displacements," J. Chem. Phys. **160**(23), 234104 (2024).
[42]V. Butkus, D. Zigmantas, L. Valkunas, and D. Abramavicius, "Vibrational vs. electronic coherences in 2D spectrum of molecular systems," Chem. Phys. Lett. **545**, 40–43 (2012).
[43]V. Butkus, L. Valkunas, and D. Abramavicius, "Molecular vibrations-induced quantum beats in two-dimensional electronic spectroscopy," J. Chem. Phys. **137**,(4), 44513 (2012).
[44]S. Hogiu, W. Werncke, M. Pfeiffer, and T. Elsaesser, "Mode specific vibrational kinetics after intramolecular electron transfer studied by picosecond anti-Stokes Raman spectroscopy," Chem. Phys. Lett. **312**(5–6), 407–414 (1999).